JOURNAL OF GEOPHYSICAL RESEARCH, VOL. 115, D00H22, doi:10.1029/2009JD012371, 2010

Comparison of high-level clouds represented in a global cloud system–resolving model with CALIPSO/CloudSat and geostationary satellite observations

Toshiro Inoue,[1] Masaki Satoh,[1,2] Yuichiro Hagihara,[3] Hiroaki Miura,[1,2,4] and Johannes Schmetz[5]

Received 30 April 2009; revised 20 October 2009; accepted 28 December 2009; published 20 May 2010.

[1] Vertical and horizontal distributions of high-level clouds (ice and snow) simulated in high-resolution global cloud system–resolving simulations by the Nonhydrostatic Icosahedral Atmospheric Model (NICAM) are compared with satellite observations. Ice and snow data in a 1 week experiment by the NICAM 3.5 km grid mesh global simulation initiated at 0000 UTC 25 December 2006 are used in this study. The vertical structure of ice and snow represented by NICAM was compared with Cloud-Aerosol Lidar and Infrared Pathfinder Satellite Observation (CALIPSO) and CloudSat observations. High-level clouds (cumulonimbus and cirrus type clouds) classified by the split window (11 and 12 μm) data on board geostationary meteorological satellites (GMSs) were used for comparison of the horizontal distributions of ice and snow in NICAM. The vertical distributions of ice and snow simulated by NICAM qualitatively agree well with those of cloud signals observed by CALIPSO and CloudSat. We computed corresponding cloud lidar backscatter coefficients and cloud radar reflectivity signals from ice and snow data of NICAM using Cloud Feedback Model Intercomparison Project (CFMIP) observational simulator packages. The contoured frequency by altitude diagram for the cloud lidar backscatter coefficients shows lower frequency at higher altitude of 8–14 km by NICAM than CALIOP observations. This suggests that the amount of ice is not well represented in NICAM. The simulated cloud radar reflectivity signals by NICAM indicated higher frequency at 8–10 km altitude than CloudSat observations, although there were some differences between over oceans and continents. This implies that the amount of snow is larger in NICAM simulations. The horizontal pattern of ice clouds (column-integrated ice and snow of greater than 0.01 kg/m^2) in NICAM shows good agreement with that of high-level clouds identified by the split window analysis. During this 1 week simulation, 48–59% of ice clouds in NICAM matches with observed high-level clouds. The cross correlation between the spatial distributions of simulated ice clouds and satellite-observed high-level clouds is 0.40–0.51, and the equitable threat score is 0.31–0.45. Furthermore, temporal variations of column-integrated ice clouds in NICAM are compared with high-level clouds classified by the split window at the decaying stage of deep convection over the tropics. The results indicate that the mean decaying speed of ice clouds of NICAM and high-level clouds by satellite observations agrees well for this analysis area and period, although the variances are larger in NICAM. This implies that the fall speed of snow in this NICAM experiment is appropriate to depict the decay of anvil clouds by compensating for the excess of snow in NICAM simulations, when we assume that the decay of anvil clouds is largely controlled by the evaporation of ice and snow.

Citation: Inoue, T., M. Satoh, Y. Hagihara, H. Miura, and J. Schmetz (2010), Comparison of high-level clouds represented in a global cloud system–resolving model with CALIPSO/CloudSat and geostationary satellite observations, *J. Geophys. Res.*, *115*, D00H22, doi:10.1029/2009JD012371.

[1]Center for Climate System Research, University of Tokyo, Kashiwa, Japan.
[2]Research Institute for Global Change, Japan Agency for Marine-Earth Science and Technology, Yokohama, Japan.

0148-0227/10/2009JD012371

[3]Center for Atmospheric and Oceanic Studies, Tohoku University, Sendai, Japan.
[4]Department of Atmospheric Science, Colorado State University, Fort Collins, Colorado, USA.
[5]EUMETSAT, Darmstadt, Germany.

1. Introduction

[2] In the Earth-atmosphere system, clouds are understood as modulating dynamics, hydrology, and radiation field. The importance of clouds and their associated processes in atmospheric models has been emphasized since the midseventies [e.g., *Arakawa*, 1975]. Recently, optically thin cirrus and low-level boundary layer clouds have been recognized as important clouds that modulate the climate system [*Stephens*, 2005]. High-level clouds generally have a cooling effect on the radiation budget. However, cirrus clouds are known to play a different role in radiative forcing than other high clouds in some cases. Cirrus clouds, which exist at higher altitude and have thinner optical thickness, warm the atmosphere more effectively [*Liou*, 1986; *Stephens*, 2005]. In the tropics, cirrus clouds are generally associated with deep convection as anvil clouds and have large impacts on the energy budget. Therefore, proper representation of cirrus clouds is one of the key issues for improving climate models. In order to ensure the reliable performance of models, better representation on various cloud properties, such as cloud fraction, cloud top height, and amounts of liquid and ice hydrometeors in the global atmospheric models are now essentially required.

[3] In general, cirrus clouds are not easily identified by satellite observations because of their semitransparent characteristics. Many methods have been proposed to detect cirrus clouds using the visible and infrared data of meteorological satellites [e.g., *Inoue*, 1985; *Prabhakara et al.*, 1988; *Rossow and Schiffer*, 1991; *Minnis et al.*, 1998; *Heidinger and Pavolonis*, 2009]. Among them, the use of split window is effective to detect long-lasting cirrus clouds from geostationary satellite data, since no visible data are required. Lidar observation is also considered a powerful tool to detect cirrus clouds and to retrieve the optical properties of cirrus clouds [e.g., *Platt*, 1979; *Sassen et al.*, 1990; *Mace et al.*, 1998a; *Okamoto et al.*, 2003]. With the launch of the Cloud-Aerosol Lidar and Infrared Pathfinder Satellite Observation (CALIPSO) and CloudSat, we now have a significant amount of new-generation observations for the vertical structure of cloud and aerosol from space. Therefore, we can use the CALIPSO and CloudSat observations to evaluate the vertical structures of ice and snow represented in global atmospheric models. We also use split window analysis to identify cirrus clouds by geostationary meteorological satellites and compare horizontal distributions and temporal variation of ice clouds appearing in global atmospheric models.

[4] Global atmospheric models are roughly categorized into climate models and numerical weather prediction (NWP) models. For evaluations of clouds simulated by climate models, long-term statistical data have been primarily used so far. One popular method is the comparison of the meridional section of zonal mean cloud properties to see whether climate models have adequate amounts of clouds [*Chepfer et al.*, 2008]. However, another approach with short-term simulations is now becoming popular, and that is targeting particular events of cloud systems for evaluations of climate models. This reflects a recent trend of the unified framework of climate and NWP models [*Davies et al.*, 2005; *Palmer et al.*, 2008]; short-term forecast skill should be better for more reliable climate simulations, and climatological fields should be better for more accurate numerical weather forecasts. Clouds with midlatitude synoptic cyclones have been examined by this approach [*Illingworth et al.*, 2007]. However, comparison of clouds in low latitudes has not been straightforward, since cloud clusters are not well represented by global atmospheric models with cumulus parameterization.

[5] A new type of high-resolution atmospheric global model, global cloud-resolving models (GCRMs), whose mesh size is a few kilometers globally, is becoming available. As an existing GCRM, *Satoh et al.* [2008] describe the Nonhydrostatic Icosahedral Atmospheric Model (NICAM) and argue that GCRMs will open a new era of research with atmospheric global models. Using the NICAM 7 km grid mesh simulation, *Miura et al.* [2007] succeeded in reproducing the realistic structure of the Madden-Julian Oscillation (MJO) event that occurred during December 2006. They also integrated NICAM for a week with 3.5 km grid mesh globally. Since this was a short-term integration, cloud systems in the tropics (cloud clusters) could be directly evaluated by observations. *Inoue et al.* [2008] statistically analyzed deep convective cloud areas in this NICAM 3.5 km grid mesh simulation over the western tropical Pacific and compared them with those of the Japanese geostationary meteorological satellite (MTSAT-1R) data. The results show that cloud coverage and the diurnal cycle of deep convection over the tropics are in good agreement between the NICAM simulation and the observation.

[6] The aim of this paper is to examine how GCRMs reproduce realistic high-level clouds, especially in the tropics. Since the simulation by *Miura et al.* [2007] was the first realistic global simulation by high resolution GCRM performed in the Earth Simulator, it is vital to know the reproducibility of clouds by this type of simulation. We compare the vertical and horizontal distributions of ice clouds between the 3.5 km grid mesh NICAM simulation and the satellite observations in sections 3.2 and 3.3. In section 3.4, we tried to argue a new approach to evaluate the behavior of simulated clouds by comparing time evolutions of high-level clouds at the decaying stage of deep convection. In section 2, the data used in this study is described and a summary of this paper is given in section 4.

2. Data

2.1. Global Cloud-Resolving Model

[7] NICAM was configured to run with an explicit cloud microphysics scheme using a mesh size of a few kilometers without cumulus parameterization [*Tomita and Satoh*, 2004; *Satoh et al.*, 2008]. Using the 7 km grid mesh NICAM, *Miura et al.* [2007] reproduced the realistic structure of an MJO event that occurred during December 2006. They also integrated a 3.5 km grid mesh NICAM globally for a week with an initial condition from the National Centers for Environmental Prediction (NCEP) Global Tropospheric Analyses at 0000 UTC on 25 December 2006 [*Nasuno et al.*, 2009]. Some aspects of deep convective clouds in this NICAM experiment have already been analyzed by *Inoue et al.* [2008] and *Masunaga et al.* [2008].

[8] In this study, we use an output data of the 3.5 km grid mesh simulation by *Miura et al.* [2007]. Although this is a short-term integration, cloud systems can be directly compared with those of the real world. Here, we focus on high-

level ice clouds including deep convective clouds and optically thin cirrus clouds. In this NICAM simulation, the cloud microphysics scheme by *Grabowski* [1998] is used. It is a simple three category scheme in which airborne and precipitating hydrometeors are prognostic variables. Cloud ice and snow are diagnosed by the temperature-dependent ratio between respective liquid and ice phases from airborne and precipitating hydrometeors. These two categories are regarded as ice clouds in this simulation. Two-dimensional fields of column-integrated and time-mean cloud ice and snow were saved every 1.5 h, while three-dimensional fields of cloud ice and snow were saved only once a day at 0000 UTC for this 3.5 km mesh experiment. We used the three-dimensional snapshot data for the comparison with the CALIPSO and CloudSat data described below.

2.2. CALIPSO and CloudSat Data

[9] The CALIPSO combines an active lidar instrument with passive infrared and visible images to probe vertical structures and properties of thin clouds and aerosols. The Cloud-Aerosol Lidar with Orthogonal Polarization (CALIOP) is a two-wavelength polarization-sensitive lidar that provides high-resolution vertical profiles of aerosol and clouds. The CALIOP measures backscatter intensity from aerosol and clouds at 532 nm and 1064 nm with 70 m horizontal resolution sampled every 333 m and 30–60 m vertical resolution [*Winker et al.*, 2007].

[10] The CloudSat is an experimental satellite that provides much needed measurements of the vertical structure of clouds and precipitation from space [*Stephens et al.*, 2002, 2008]. The Cloud Profiling Radar (CPR) on board CloudSat is a 94 GHz nadir-looking radar that measures the power backscattered by clouds. Spatial resolution of the CPR data is sampled at 1.7 km along track and 1.3 km across track and vertical resolution is 480 m oversampled at 240 m. Calibration accuracy of CPR is 1.5 dB.

[11] CALIPSO and CloudSat fly in formation with three other satellites as the A-train constellation [*Stephens et al.*, 2002]. The observation time lag is about 15 s between CALIPSO and CloudSat. The level 1-b data of CALIPSO and CloudSat were used in this study. Both CALIPSO and CloudSat data were gridded onto a 0.05 degrees latitude/longitude grid map by selecting the nearest neighbor pixel with original vertical resolution.

2.3. Split Window (11 and 12 μm) Data

[12] Using the split window data, *Inoue* [1987, 1989] developed a simple cloud type classification method. *Inoue* [1985] found that brightness temperature difference between the 11 and 12 μm (BTD) become larger for cirrus cloud due to differential absorption by ice between the two wavelength. The BTD becomes larger for cirrus clouds, although the BTD depends on optical thickness and effective radius of ice particle. The method can basically classify optically thin cirrus clouds that consist of ice and optically thick clouds utilizing the differential absorption by ice between 11 and 12 μm. *Inoue* [1997] compared the cloud type classified by the split window and optical thickness by International Satellite Cloud Climatology Project (ISCCP). He showed that mean optical thickness for thin cirrus, thick cirrus, low-level cumulus/stratocumulus and cumulonimbus type cloud classified by the split window are 2.2, 7.4, 15.3 and 33.7. *Inoue and Ackerman* [2002] studied the radiative effect of each cloud type classified by the split window using the coincident and collocated Earth Radiation Budget Experiment (ERBE) data. They showed that low-level cumulus/stratocumulus type cloud and cirrus type cloud indicated similar values in longwave fluxes, however, low-level cumulus/stratocumulus type clouds indicated very large shortwave fluxes, while cirrus type clouds indicated very low values in shortwave fluxes. These characteristics are reasonable for each cloud type. Further they showed that some of the cirrus type clouds classified by the split window indicate positive net cloud radiative forcing (warming) at the top of the atmosphere.

[13] In this study, cloud type classification was performed based on the diagram used by *Inoue et al.* [2009]. We arbitrarily classify cloud types depending on the brightness temperature (TBB: at 11 μm) and BTD. The TBB is a good indicator for cloud top temperature for optically thick clouds, while the BTD is a good indicator to classify optically thin cirrus type clouds that consists of ice [*Inoue*, 1987]. We select three TBB thresholds of 213K, 253K and clear TBB to assign very high/high/middle and low clouds. Here, the clear TBB was determined as the maximum TBB within 1° latitude/longitude area between 0000 UTC 26 December 2006 and 0000 UTC 1 January 2007. We also select three BTD thresholds as 1K, and clear BTD to assign optically thicker clouds and ice clouds. Here, the clear BTD was determined as the BTD corresponding to clear TBB. We define high-level clouds as clouds colder than 253K of TBB, which corresponds to 8 km in the U.S. tropical standard atmosphere, and cirrus type clouds that are warmer than 253K with larger BTD.

[14] Calibration accuracy is essential in cloud type classification, since our cloud type classification uses the brightness temperature difference between 11 and 12 μm. Under the Global Space-based Inter-Calibration System (GSICS) program organized by *World Meteorological Organization* [2006], each Agency is processing intercalibration between geostationary satellite and low-orbit satellite. The split window data from the U.S. Geostationary Operational Environmental Satellite (GOES-W) and the European geostationary satellite (METEOSAT-8) were used to identify high-level clouds in this study, since the calibration accuracy is reasonable for these satellites. The split window data were also gridded onto a 0.05 degrees latitude/longitude grid map.

3. Results

3.1. Comparison Between Split Window Analysis and CALIPSO Data

[15] Here, we first studied the effectiveness of the split window analysis. Clouds warmer than 253K are used to be classified as middle- or low-level cloud in a single infrared analysis. However, optically thin semitransparent cirrus cloud TBB is often warmer than 253K, which is warmer than the temperature where cirrus clouds exist. The split window analysis utilizes the BTD to detect cirrus type clouds. Figure 1 shows the frequency in percentage in the TBB-BTD diagram for the clouds higher than 8 km by CALIOP observation. The percentage in the diagram is shown for each category of TBB (<253K, 253K–273K, >273K). The diagram is constructed from only the clouds that are higher than 8 km in CALIOP observations from 30 orbits over the GOES-W observation

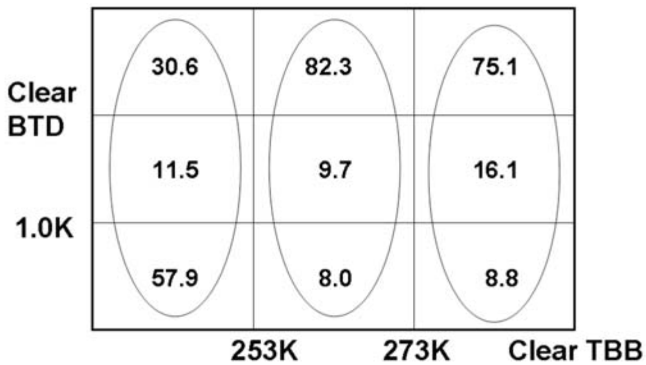

Figure 1. Frequency in percentage in TBB-BTD diagram, for clouds that have CALIOP signals higher than 8 km. Frequency is computed for categorized TBB (<253K, 253K–273K, >273K) shown by ellipsoids. The numbers in each column add up to 100, i.e., 100%. The diagram was constructed from 30 orbits that match within 30 min observation time between CALIOP and GOES-W during 26–31 December 2006.

area. Sample number of each TBB category is 4541, 1436 and 2018. Beyond the TBB warmer than 253K, the frequency becomes higher over larger BTD in this diagram. This diagram shows 75% (82%) of clouds warmer than 273K (253K–273K) indicate larger BTD. This region in the diagram corresponds to the cirrus type clouds in split window analysis. Generally, clouds warmer than 253K are middle- or low-level cloud in the single infrared cloud type classification. Using the split window, we can detect cirrus clouds among these clouds even when clouds are warmer than 273K.

[16] Clouds in the region of colder than 253K TBB in the diagram correspond to high-level clouds of cumulonimbus type clouds or thick cirrus clouds. Depending on cloud type the BTD in this region also shows some variety, although the percentage of smaller BTD (optically thicker) clouds indicates higher values of 58%.

[17] Thus, Figure 1 demonstrates that clouds higher than 8 km observed by CALIOP are mostly classified as cumulonimbus type or cirrus type by the split window. This is consistent with the research by *Hamada et al.* [2008], which studied upper tropospheric clouds observed by ship-borne cloud radar and by the split window of GMS-5. Some examples of correspondence between high-level clouds by split window and CALIOP observations are shown in sections 3.2 and 3.3.

3.2. Case 1, 0000 UTC 26 December 2006

3.2.1. Spatial Distributions of Ice Clouds in NICAM and Split Window Analysis

[18] Figure 2a illustrates an example of high-level clouds classified by the split window over the area covered by GOES-W at 0000 UTC 26 December 2006. The backscatter coefficients by CALIOP observations and cloud radar reflectivity by CloudSat observations along this orbit (an orange line in Figure 2a) are shown in Figures 3a and 3b. The lower limit of CALIOP backscatter coefficients in Figure 3a was set to 0.0075 km^{-1} sr^{-1} to detect thinner cirrus based on the findings by *Liu et al.* [2004], although it is slightly noisy because of day time observation. High-level clouds classified by the split window are seen along the orbit over 50°N (area A), 30°N (area B), 5°N (area C), 10°S–20°S (area D), 30°S–40°S (area E), and 57°S (area F) in Figure 2a. The cloud tops of these clouds (areas C, D, E, F) correspond well to the cloud signals higher than 8 km by CALIOP and cloud radar observations (Figures 3a and 3b), although the clouds (areas A and B) over higher latitude than 30°N are slightly lower than 8 km.

[19] In Figure 2b, we now show the spatial distribution of column-integrated cloud ice and snow represented in the NICAM 3.5 km grid mesh simulation [*Miura et al.*, 2007] at 0000 UTC 26 December 2006 to compare with high-level clouds by the split window analysis of GOES-W (Figure 2a). *Wylie et al.* [1995] suggested that optical thickness of 0.3 was the lower limitation of cirrus retrieval from satellite measurements. *Ackerman et al.* [2008] indicated that the Moderate Resolution Imaging Spectroradiometer (MODIS) cloud mask algorithm was sensitive to clouds with an optical thickness greater than 0.4. Thus, we plot the area containing column-integrated ice and snow contents greater than 0.01 kg m^{-2} that roughly corresponds to 0.4 in optical thickness.

[20] We can see good agreement of high-level cloud area in Figure 2a and column-integrated ice and snow area in Figure 2b. For example, deep convective clouds over the Intertropical Convergence Zone (ITCZ) and the South Pacific Convergence Zone (SPCZ), clouds over North America, and clouds over 40°S–50°S are captured in both results. In Figure 2a, the purple, blue, green and yellow colors illustrate respective clouds colder than 213K, cumulonimbus type clouds, thicker cirrus colder than 253K and optically thinner ice clouds. On the other hand, in Figure 2b, the color corresponds to the amount of vertically integrated ice and snow simulated in NICAM; where purple color indicates a larger amount, while green and yellow color indicates a smaller amount of column-integrated ice and snow. The larger amount of column-integrated ice and snow area in NICAM generally corresponds to cumulonimbus type clouds classified by the split window, while a smaller amount of ice and snow area in NICAM generally corresponds to optically thin cirrus clouds classified by the split window. There are of course some discrepancies between the simulation and the observation.

[21] We determine the ability of NICAM for reproducing high-level clouds using the whole area of Figure 2 by assuming the satellite observations as truth. A contingency table was constructed, showing the number of times cloud occurred in both NICAM and satellite (area A), the number of times cloud occurred in neither NICAM nor satellite (area D), and the number of times that cloud occurred in either NICAM or satellite but not both (areas B and C). The simple scores, probability of detection (POD) = A/(A + C) and false alarm ratio (FAR) = B/(A + B), were computed [e.g., *Mace et al.*, 1998b]. The POD was 59% and FAR was 27% for this case. The cross correlation between the two was 0.51 and the equitable threat score (ETS) = $(A - E)/(A + B + C - E)$, where $E = (A + B)(A + C)/(A + B + C + D)$ [*Illingworth et al.*, 2007], was 0.45. The scores for 6 days over this area are shown in Figure 4. As is expected, these scores become worse over time, in particular the temporal change of FAR becomes worse than POD.

3.2.2. Vertical Distributions of Ice and Snow in NICAM and CALIPSO/CloudSat Observations

[22] Since vertical distributions of cloud ice and snow were saved only once a day in this experiment, the number

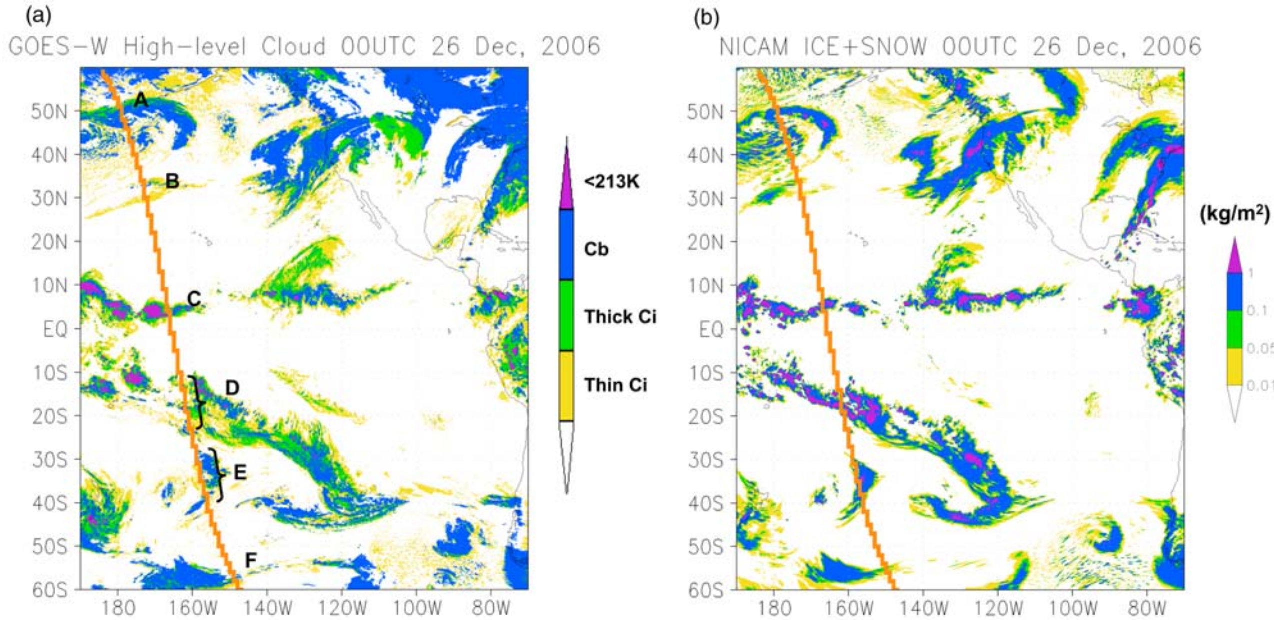

Figure 2. Horizontal distributions of high-level cloud classified by the split window of (a) GOES-W and of (b) column-integrated ice and snow (kg m^{-2}) simulated by NICAM. Time is 0000 UTC 26 December 2006. In Figure 2a, clouds colder than 213K, cumulonimbus-type clouds, thick cirrus-type clouds, and thin cirrus-type clouds are shown as <213 (purple), Cb (blue), thick cirrus (green), and thin cirrus (yellow), respectively. The CALIPSO orbit is also shown by an orange curve in Figures 2a and 2b. Typical high-level cloud areas are labeled as A to F in Figure 2a.

of coincident comparisons between the observations of CALIPSO and CloudSat with NICAM are limited. Figures 5a and 5b show vertical profiles of ice and snow (mixing ratio; kg/kg) represented in NICAM along the orbit in Figure 2a. Comparing Figures 5a and 5b and Figures 3a and 3b, we can see good correspondence between the vertical and latitudinal profiles of ice and snow in NICAM and those of observed cloud signals by cloud lidar and cloud radar. In this experiment, we note that ice amount is much smaller than snow amount, since the color bar indicates a difference of 10 times.

[23] To quantify the comparison, we can compute the corresponding lidar and radar signals using the CFMIP Observational Simulator Package (COSP; see http://cfmip.metoffice.com/COSP.html) [*Haynes et al.*, 2007; *Chepfer et al.*, 2008; *Bodas-Salcedo et al.*, 2008] version 1.1. We use the vertical profiles of cloud properties together with ther-

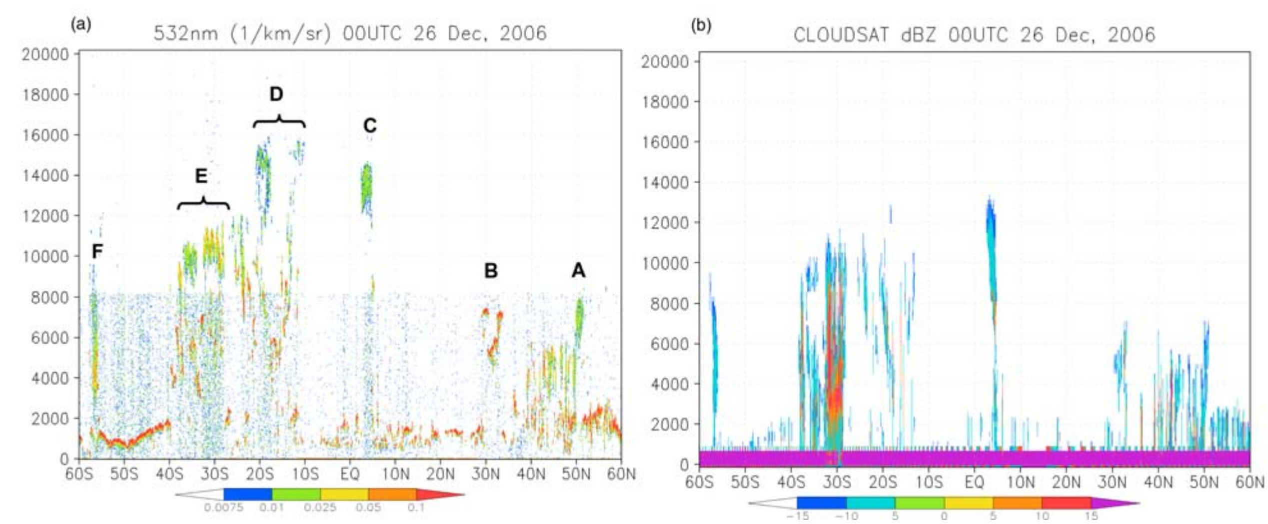

Figure 3. (a) Backscatter coefficients (km^{-1}sr^{-1}) at 532 nm observed by CALIOP and (b) reflectivity (dBZ) observed by cloud radar on board CloudSat along the orbit in Figure 2a. Cloud signals labeled A to F in Figure 3a correspond to high-level cloud areas in Figure 2a.

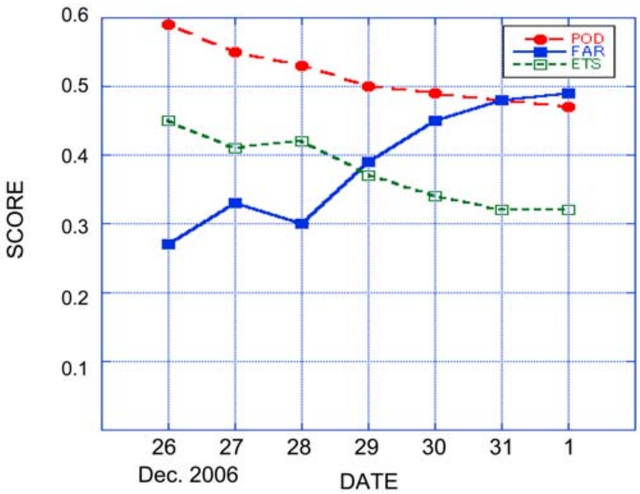

Figure 4. Temporal variations of POD, FAR, and ETS computed over the area of Figure 2a from 0000 UTC 26 December 2006 to 0000 UTC 1 January 2007 over GOES-W area.

modynamic variables produced by NICAM, assuming 10μm for liquid clouds and 40 μm for ice clouds. However, we found that the simulated lidar signals are sensitive to the size of cloud ice assumed in COSP. The results are shown by Figures 6a and 6b, which correspond to the respective cross sections shown by Figures 3a and 3b. In computation of lidar signals, we use both ice and snow data in NICAM. We can see a clearer similarity of vertical and latitudinal profile between simulated and observed. The CALIOP observations can generally detect signals near the cloud top for deep convective clouds over 5°N (cloud area C in Figure 3a). This feature is also simulated.

3.2.3. Vertical Distributions of Ice and Snow in NICAM and CALIPSO/CloudSat Observations Over GOES-W Coverage

[24] For statistical comparison, we constructed contoured frequency of altitude diagrams (CFAD) using the data higher than 4 km in altitude over 30°S–30°N because we focused on high-level cloud in this study. The CFAD that show the two-dimensional frequency of occurrence in altitude and signal strength are generally used to diagnose the simulated cloud in comparison with satellite observations [*Masunaga et al.*, 2008]. The vertical distributions of ice and snow simulated by NICAM were saved once a day at 0000 UTC. However, day orbit of CALIPSO and CloudSat passed over the Pacific Ocean around 0000 UTC (less than 1 h difference) during these days. Thus, we construct mean CFAD using six orbits data to study the structure of high-level cloud over ocean. *Masunaga et al.* [2008] used CFAD of cloud radar and precipitation radar to study NICAM performance. Here we used the CFAD of cloud lidar and cloud radar.

[25] Figure 7 shows the mean CFAD for simulated lidar signals (Figure 7a), CALIOP observations (Figure 7b), difference (NICAM – CALIOP) (Figure 7c), simulated radar signals (Figure 7d), CloudSat observations (Figure 7e), and difference (NICAM – CloudSat) (Figure 7f). Simulated lidar signals (Figure 7a) show double peaks in frequency centered at 10 km altitude and backscatter coefficients of 0.01 km^{-1} sr^{-1} and 0.005 km^{-1} sr^{-1}. CALIOP observations (Figure 7b) show similar distribution patterns with semidouble peaks in CFAD, although the peak at the weaker backscatter coefficient is not significant. The simulated lidar signal is slightly lower than CALIOP observations at higher backscatter coefficient. Figure 7c shows less frequency at higher altitude and a stronger backscatter coefficient region in CFAD by NICAM simulation. As seen in section 3.2.2, this also suggests that the amount of ice is not well represented in NICAM at higher altitude.

[26] The simulated radar signals (Figure 7d) show a robust higher frequency at 8–10 km altitude and slightly higher frequency at lower altitude and stronger radar reflectivity. While corresponding CloudSat observations showed an arc-like structure of higher frequency in CFAD as given by *Masunaga et al.* [2008]. The distribution pattern is similar for both simulated and observed, however, the difference between the two (Figure 7f) shows clear higher frequency at 8–10 km altitude by NICAM and lower frequency at 5–8 km altitude with stronger radar reflectivity region in CFAD. This suggests an excess of snow with larger particle size at higher altitude, which is discussed by *Masunaga et al.* [2008].

3.3. Case 2, 0000 UTC 29 December 2006

3.3.1. Spatial Distributions of Ice Clouds in NICAM and Split Window Analysis

[27] From the limited available three-dimensional data, we chose another case at 0000 UTC 29 December 2006. At this time, the orbit of CALIPSO overlaps with the METEOSAT-8 observational domain. A comparison of the cloud properties of NICAM and METEOSAT-8 is shown in Figure 8. The color code is the same as in Figure 2. Even though this is the fourth day of the integration from the initial condition, it shows that size and location of cloud clusters in the tropics are in good agreement between the simulation and the observation. In particular, cloud areas classified by the split window over the southern part of Africa, southwestern part of northwest of Africa and the southeastern part of east of Brazil indicate remarkable correspondence with the higher amount of column-integrated ice and snow simulated by NICAM.

[28] Again in this case, we compute the reproducibility of ice clouds by NICAM assuming that the satellite observation is truth. The POD by NICAM computed from the whole area of Figure 8 was 53% and the FAR was 49%. The cross correlation between the two was 0.41 and the equitable threat score was 0.39. The scores were worse than those of Case 1 since the integration time was longer in Case 2 (the fourth day) than in Case 1 (the first day) and large land exists in this area.

3.3.2. Vertical Distributions of Ice and Snow in NICAM and CALIPSO/CloudSat Observations

[29] Figure 9 shows the cross sections of the backscatter coefficients at 532 nm of CALIOP (Figure 9a) and those of the cloud radar reflectivity of CloudSat (Figure 9b) along the orbit (orange curve) shown in Figure 8. The time difference between the NICAM data and the satellite observations is less than 15 min. The cloud signals of CALIOP and CloudSat are seen at higher altitude over the latitudes around 50°N (area G), 5°N–25°S (area H), and 50°S (area I). At these latitudes, NICAM reasonably represented larger amounts of ice and snow as seen in Figures 10a and 10b. Here, we again note that the color scale is 10 times larger for snow.

[30] To make the comparison clearer, we show the cross sections of lidar and radar signals simulated by COSP in

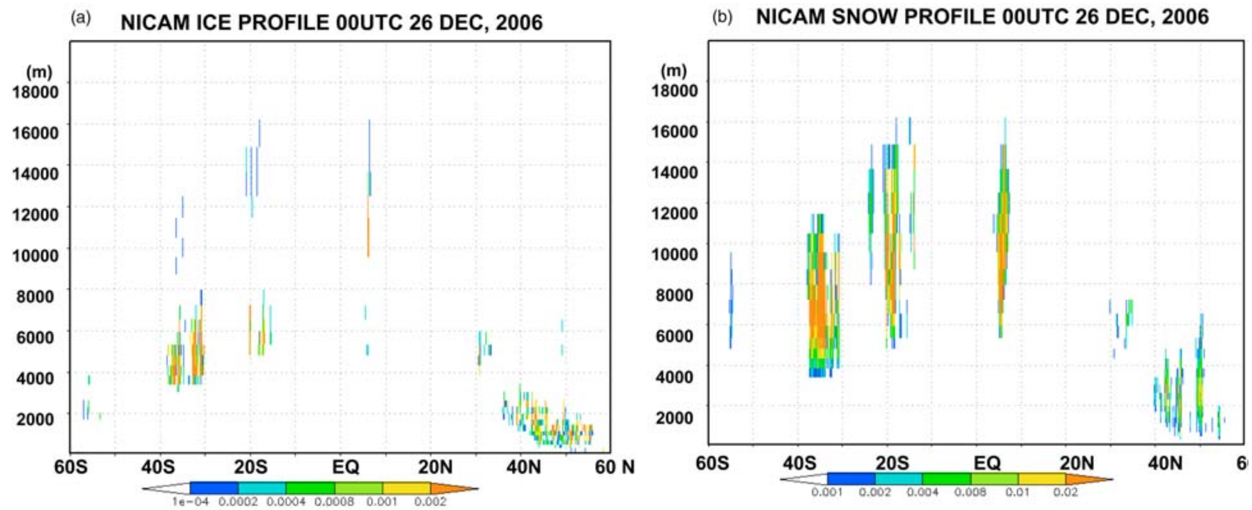

Figure 5. Vertical profile of mixing ratio (kg/kg) of (a) ice and (b) snow simulated by NICAM along the orbit in Figure 2a.

Figure 11. The vertical and latitudinal profile of simulated cloud lidar backscatter coefficient and cloud radar reflectivity correspond well to those of the cloud signals by CALIOP and CloudSat, especially over the latitudes near 50°N, 5°N–25°S, and 50°S. We found that the simulated lidar signals are sensitive to the size of cloud ice, however, the simulated feature corresponds well to the observations with the default mode. The simulated radar signals also show reasonable agreement with the CloudSat observations.

3.3.3. Vertical Distributions of Ice and Snow in NICAM and CALIPSO/CloudSat Observations Over Meteosat-8 Coverage

[31] The CFAD for lidar backscatter coefficients and radar reflectivity over 30°S–30°N is constructed using 6 night orbits over Meteosat-8 coverage during the experiment period and shown in Figure 12. The distribution pattern of lidar is similar between the simulated (Figure 12a) and the observed (Figure 12b) as seen in Figure 7 with double peaks in CFAD. In the Meteosat-8 coverage area, the weaker backscatter coefficient is more dominant than the GOES-W coverage. The peak of frequency is slightly higher altitude (13 km) in CALIOP observations over the Meteosat-8 coverage area than the GOES-W coverage area. Although the higher-frequency altitude is similar to the GOES-W coverage, the NICAM simulated higher-altitude signals over this Meteosat-8 coverage, where it seems to be affected by the African continent. Again, frequency at higher altitude and stronger backscatter coefficient in NICAM is smaller. This suggests that ice production in NICAM is less at higher altitude.

[32] The arc-like feature of higher frequency is seen in CloudSat observations (Figure 12e) as in Figure 7, however, the simulated signals (Figure 12d) are rather flat in altitude

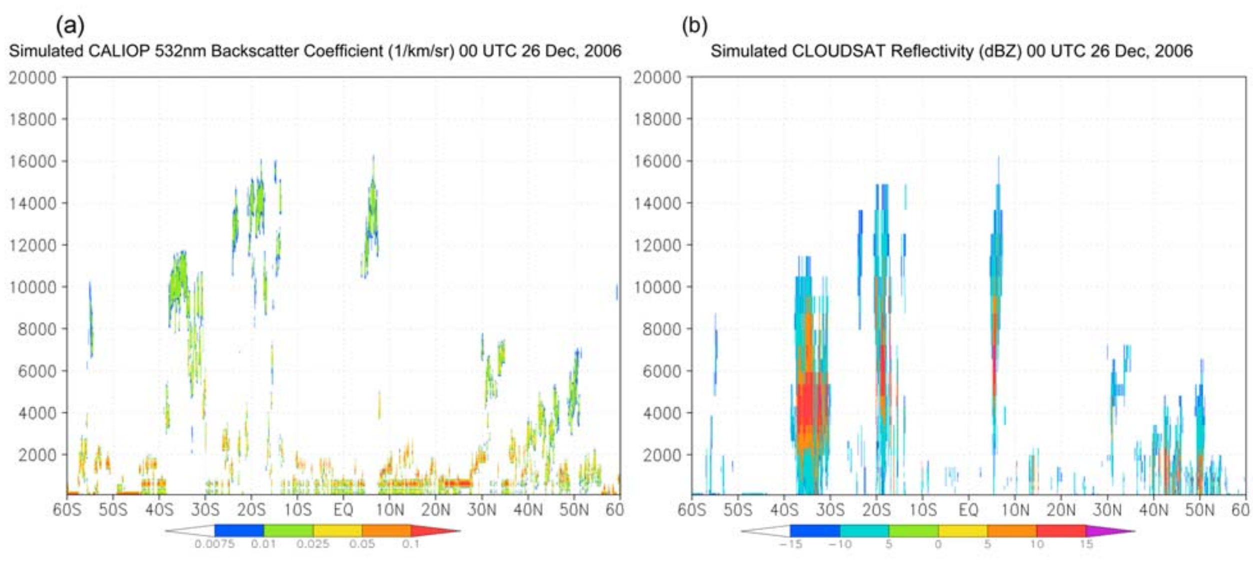

Figure 6. (a) Simulated cloud lidar backscatter coefficients and (b) simulated cloud radar reflectivity using NICAM cloud properties along the orbit in Figure 2a.

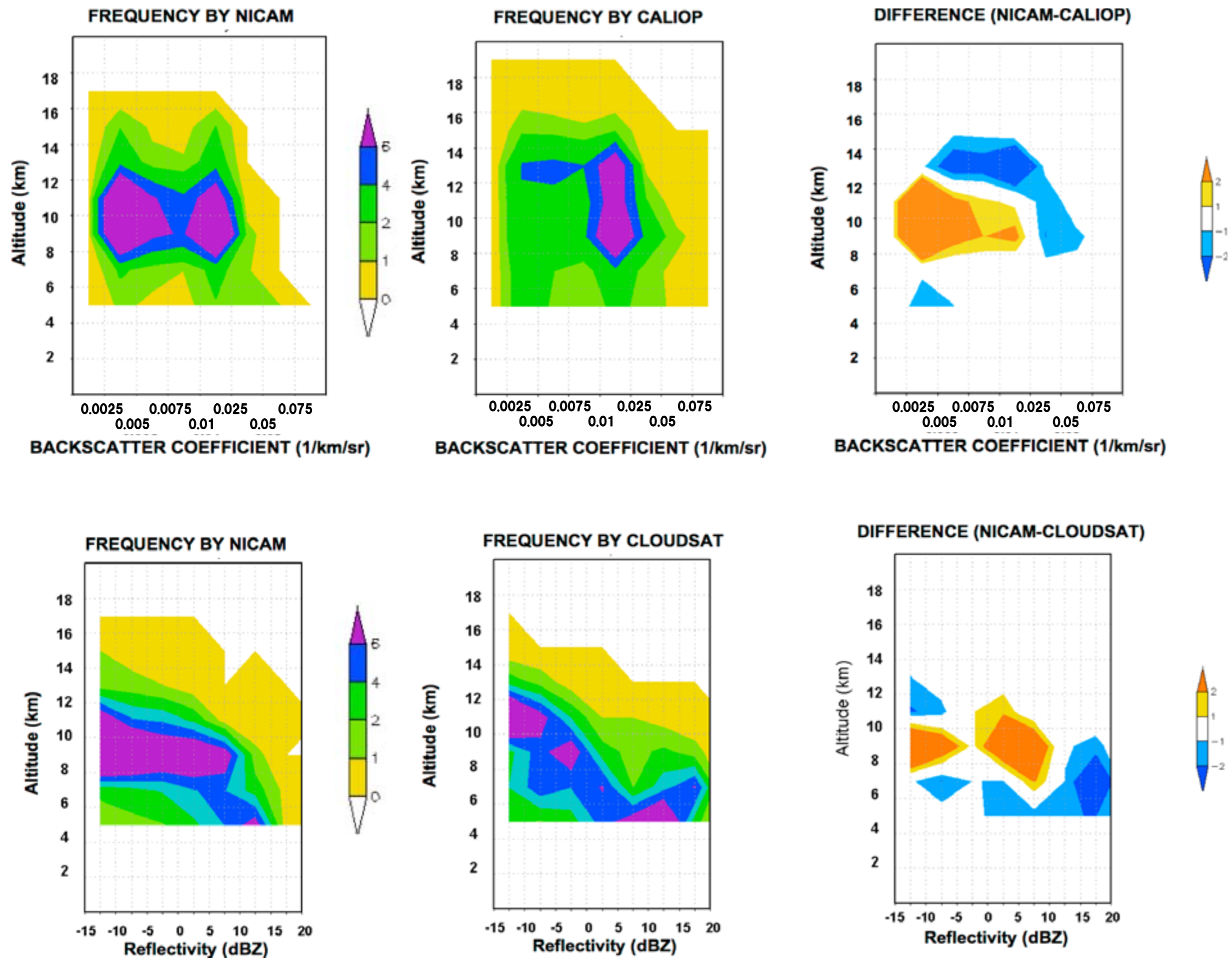

Figure 7. The contoured frequency of altitude diagrams (CFAD; %) of backscatter coefficient height for (a) NICAM simulation, (b) CALIOP observation, and (c) difference (NICAM – CALIOP) and those of reflectivity for (d) NICAM simulation, (e) CloudSat observation, and (f) difference (NICAM – CloudSat) over 30°N–30°S GOES-W coverage constructed from six day orbits around 0000 UTC during 26–31 December 2006.

at 8–10 km, which is similar to that over GOES-W area. The frequency of simulated radar reflectivity is lower than CloudSat observations over higher altitude and the weaker reflectivity region in the CFAD (Figure 12f) is also seen. The simulated signals show higher frequency at 5–10 km altitude with 0–10 dBZ, although not so clear as in Figure 7. This suggests that larger amount of snow is produced by NICAM simulation.

3.4. Temporal Variation of High-Level Cloud at the Decaying Stage of a Deep Convective System

[33] Although the NICAM simulation is not intended to predict the precise location of each individual deep convective cloud, we have seen that the location and shape of cloud clusters defined by outgoing longwave radiation (OLR) are very similar to those of the satellite observations [e.g., *Inoue et al.*, 2008]. Here, we also see the similarity between the spatial distributions of ice clouds in this NICAM experiment and that of high-level clouds by split window analysis. To trace the temporal variations of high-level clouds, we show 6-hourly spatial distributions of high-level clouds over 40°N–40°S in GOES-W coverage in Figure 13, and those of the ice clouds by NICAM over the same area in Figure 14. The time varies from Figures 13a to 13d and from Figures 14a to 14d. There are several similarities in shape such as the cloud areas labeled as A and B in Figures 13a and 14a. Thus, we can trace these cloud areas in the sequential images of Figures 13b and 14b, Figures 13c and 14c and Figures 13d and 14d as labeled A′ and B′. We also notice that the decay of cloud size in terms of time is almost the same for both NICAM and satellite observations.

[34] Temporal variations of the size of deep convection over the tropics have been studied using satellite data [*Machado et al.*, 1998; *Luo and Rossow*, 2004; *Kondo and Nakamura*, 2006; *Inoue et al.*, 2009]. They all showed that the size of deep convection shrank at the decaying stage. Here, we tried to study the decaying rate of the size of deep convection including anvil clouds using sequential images with 3-hourly intervals. The ratio of cloud size to the maximum cloud size during the life cycle was computed for isolated deep convections. We compute the number of grid points (0.05 degree lat/lon) enclosed by the threshold value of 0.01 kg m^{-2} for

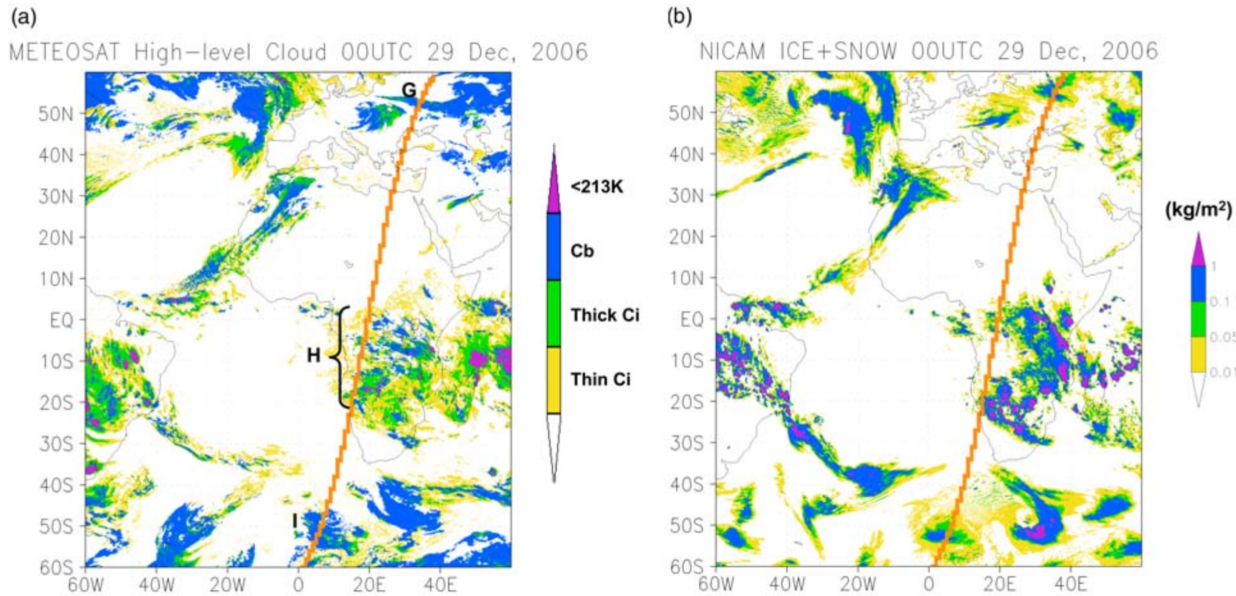

Figure 8. Same as Figure 2 but for (a) METEOSAT and (b) NICAM. Time is 0000 UTC 29 December 2006. Typical high-level cloud areas are labeled G to I in Figure 8a.

NICAM, and high-level cloud area classified by the split window for each sequential image.

[35] Figure 15 shows the temporal variation of high-level cloud area after the maximum size appeared during the life cycle of deep convection. The cloud area is represented as the ratio of area size to the maximum area size. Squares and solid line bars indicate mean and standard deviations computed from 17 cases selected from NICAM, while dots and dotted bars indicate mean and standard deviation for 11 cases selected from satellite observations during the analysis period. Selected deep convections are independent in the NICAM simulation and the satellite observation. Both the NICAM simulation and the satellite observation show a quite similar temporal tendency in shrinking the size at the decaying stage, although NICAM indicates a larger variance with time. It is interesting to note that the variance is smaller in satellite observations. The decay of anvil clouds in real world might be complicated depending on the meteorological parameters around the cloud area [e.g., *Yuter and Houze*, 2003; *Luo and Rossow*, 2004; *Horvath and Soden*, 2008]. However, this result suggests that the fall speed of snow in this NICAM experiment is appropriate to compensate the excess snow produced by NICAM, when we select the purely decaying anvil cloud that is largely controlled by the evaporation of ice and snow. It should be noted, however, that we need more careful analysis to identify the precise timing of the cloud area evolution by a statistical approach.

[36] We only show a small number of cases because of the limited data of this experiment, and it is therefore perilous to come to a general conclusion. Here, we simply show one

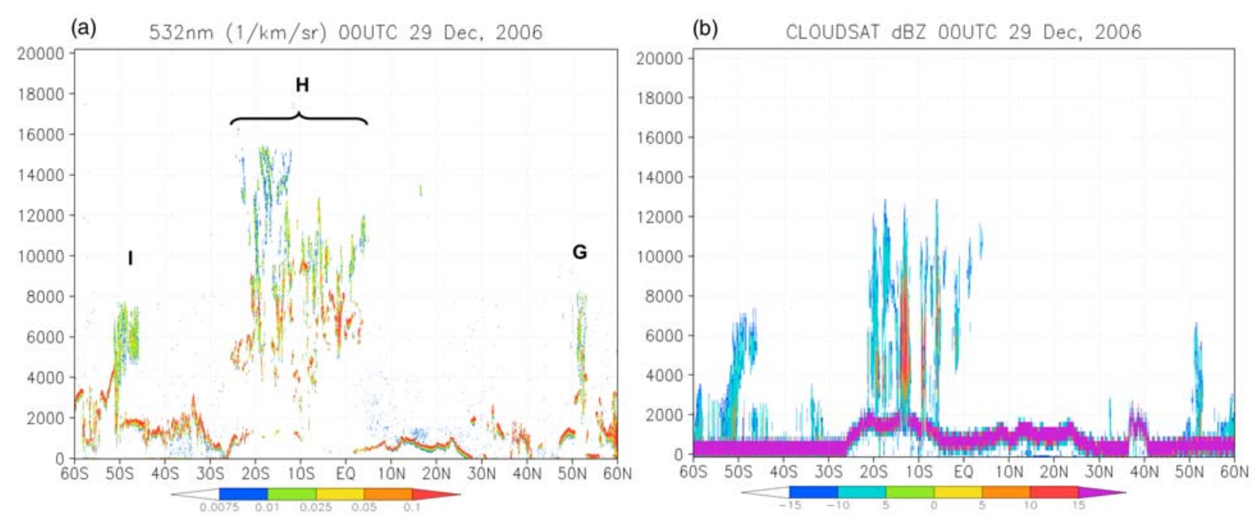

Figure 9. Same as Figure 3 but for the orbit in Figure 8a. Cloud signals G to I correspond to high-level cloud areas in Figure 8a.

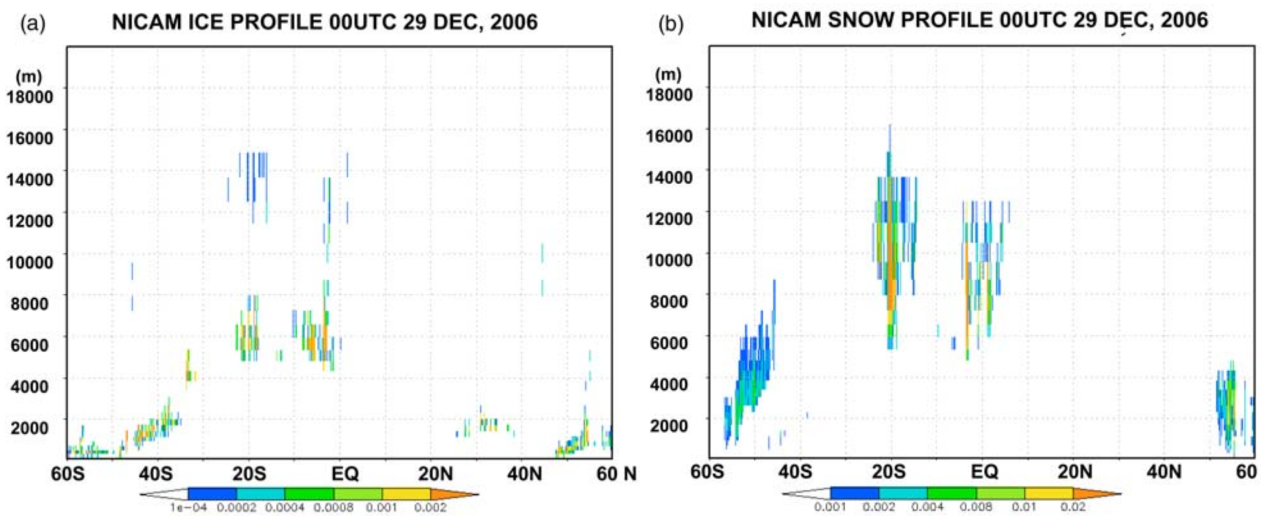

Figure 10. Same as Figure 5 but for the orbit in Figure 8a.

possible approach for the improvement of cloud microphysics schemes. The combination of the comparisons of CFAD and of the time evolutions of cloud areas somewhat isolate the cause of the discrepancy, and give insight into cloud microphysics schemes. We therefore require a larger amount of samples to discuss more statistical results.

4. Concluding Remarks

[37] *Miura et al.* [2007] conducted a global cloud system–resolving simulation for a week using NICAM with 3.5 km grid mesh globally using Earth Simulator. Although this simulation was a short-term integration, the GCRM has many grid points that can give data for a statistical comparison and cloud systems in the tropics (cloud clusters) could be directly compared with those of satellite observations. Three-dimensional distributions of cloud configuration defined by ice and snow in NICAM were compared with high-level clouds classified by the split window from geostationary satellites and with the CALIPSO/CloudSat observations. Both categories of ice and snow, in the cloud microphysics scheme of NICAM are regarded as ice clouds (high-level clouds) in this study.

[38] The vertical profiles of ice and snow by NICAM compared with the CALIPSO and CloudSat observations along the orbit. The latitudinal position and height of ice and snow by NICAM correspond well to the respective lidar/radar signals by CALIOP and CloudSat. The lidar and radar simulations of COSP are used to make a clear comparison between the NICAM cloud properties and the CALIOP and CloudSat observations. Cloud lidar simulations with default particle size show good agreement with CALIOP observations, although we found the dependency on cloud particle size for satellite simulators. Cloud radar simulations suggest that excessive large particle size snow production in NICAM as discussed by *Masunaga et al.* [2008].

[39] The spatial distributions of ice clouds (column-integrated ice and snow of greater than 0.01 kg/m^2) by

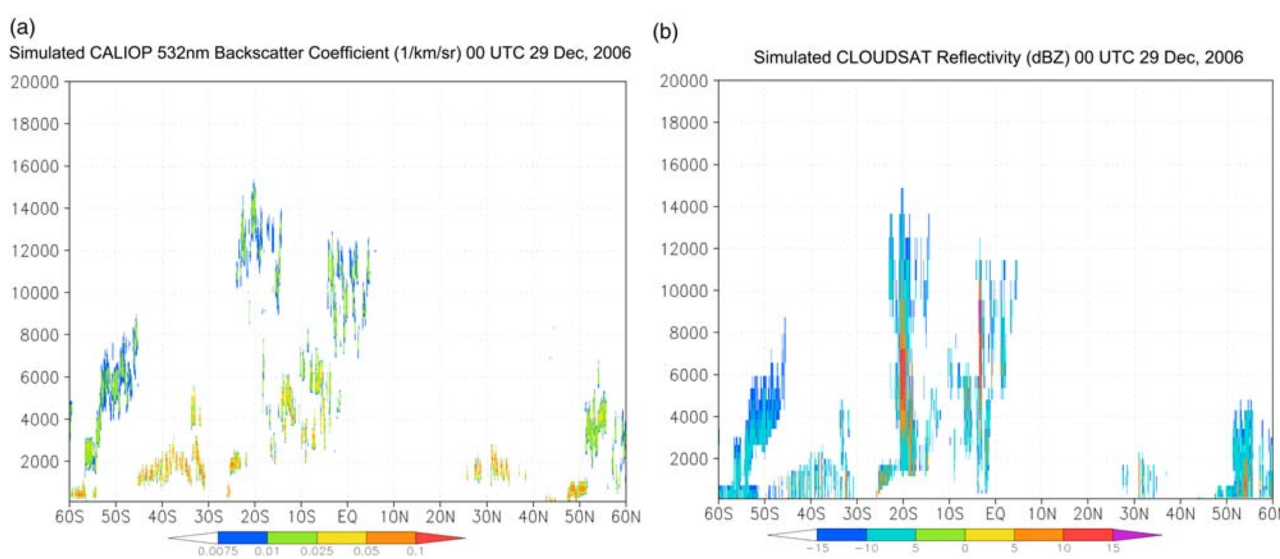

Figure 11. Same as Figure 6 but for the orbit in Figure 8a.

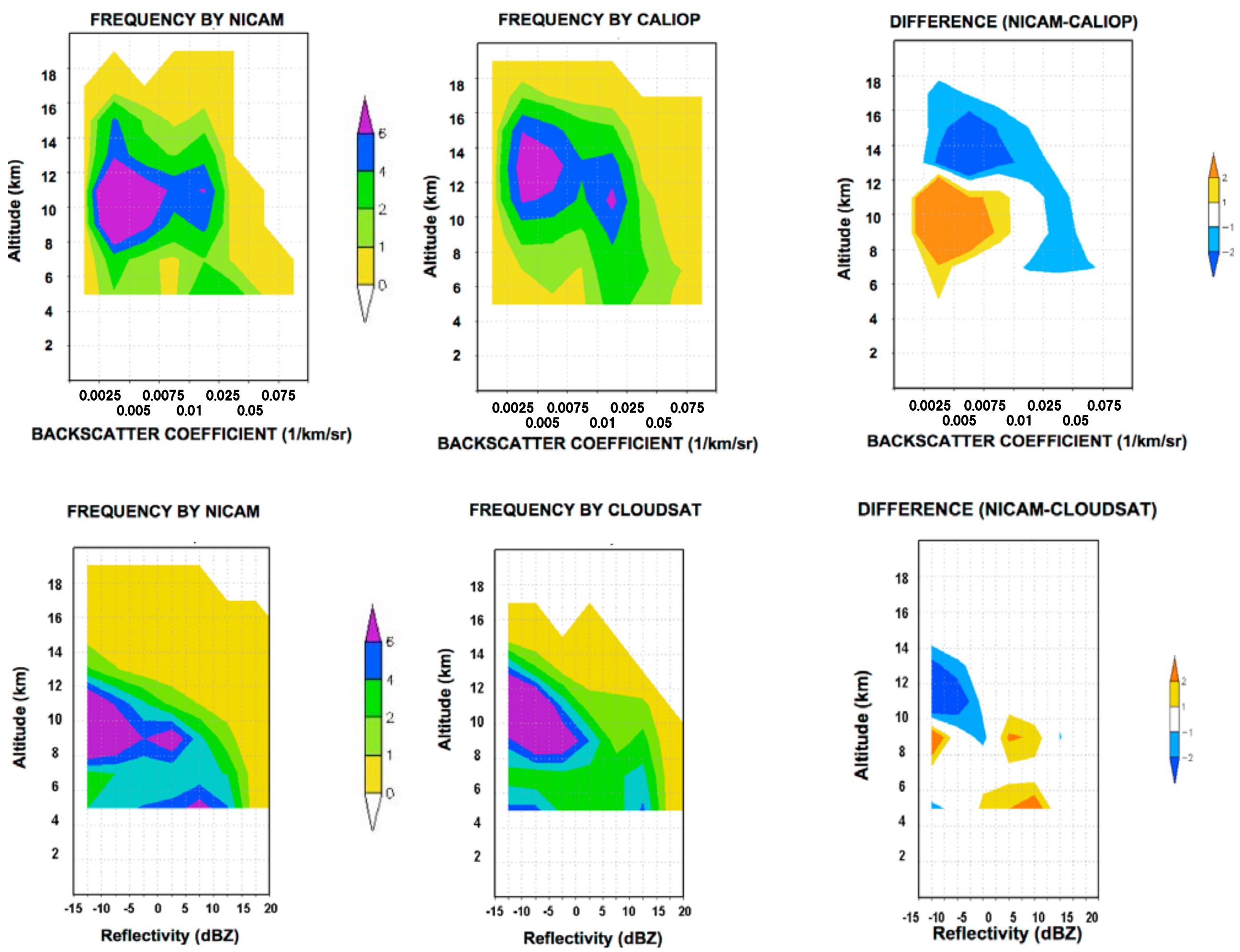

Figure 12. Same as Figure 7 but for six night orbits over Meteosat-8 coverage.

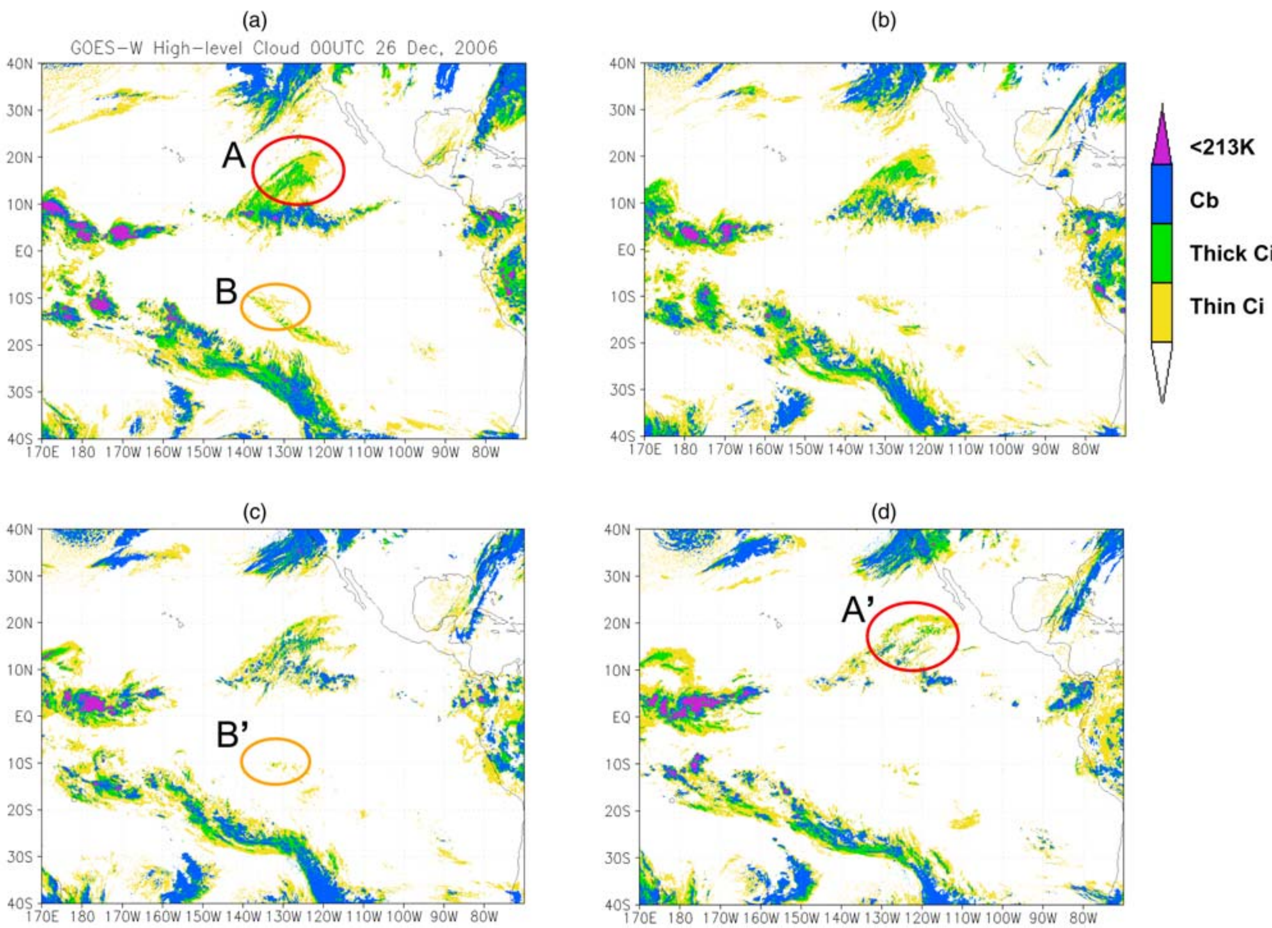

Figure 13. Six-hourly images of high-level cloud classified by the split window over 40°N–40°S GOES-W coverage starting at 0000 UTC 26 December 2006 (time goes from left to right and top to bottom).

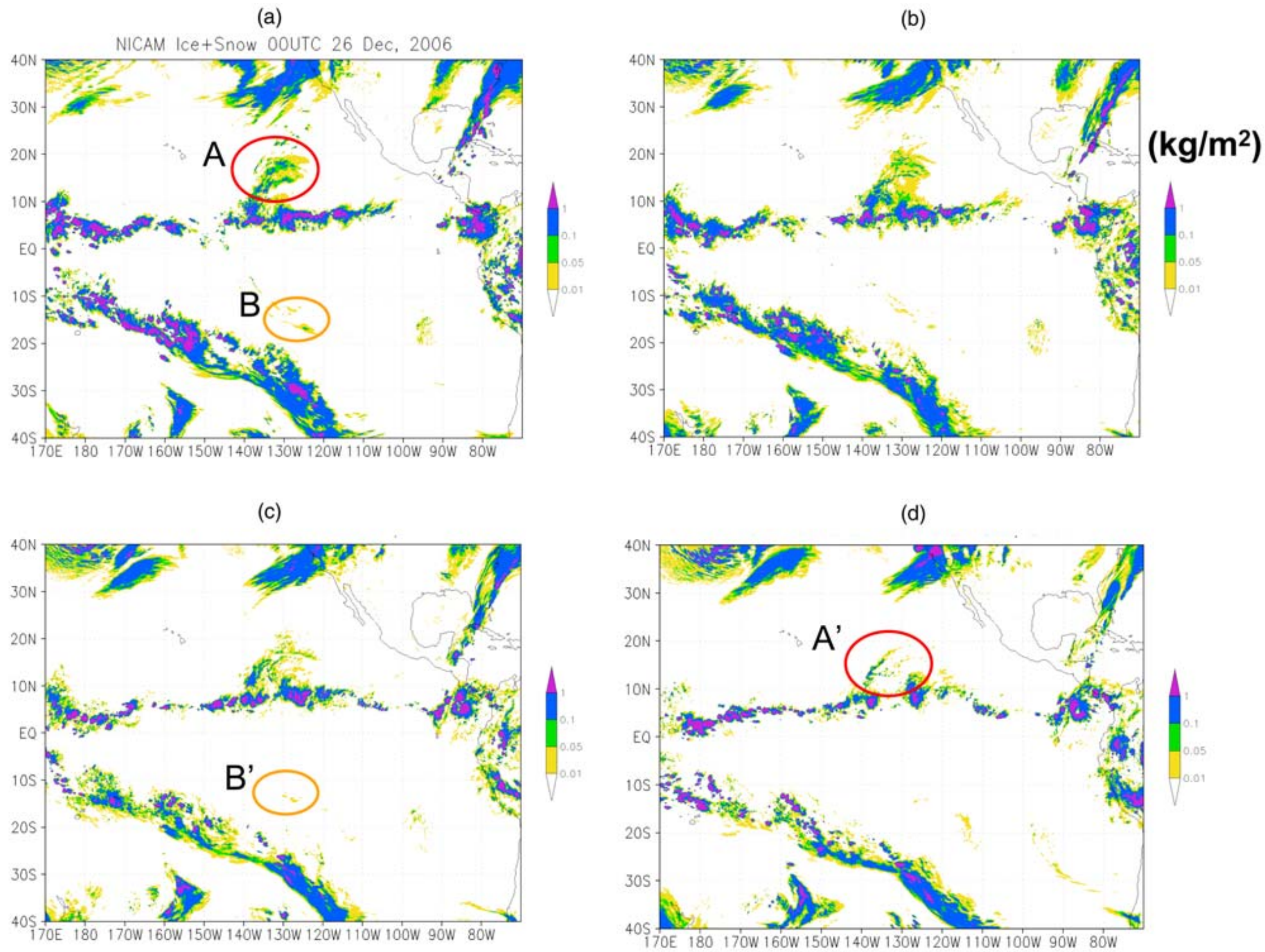

Figure 14. Same as Figure 13 but for ice clouds in NICAM.

NICAM agreed well with those of high-level clouds classified by the split window. If the satellite observations are assumed to be truth, the NICAM simulation indicates a 48–59% probability of detection and a 27–49% false alarm ratio during the 6 days from 26 December 2006 over the GOES-W observation area. The cross correlation between the spatial distributions of simulated ice and snow areas and satellite observed high-level clouds is 0.40–0.51, and the equitable threat score is 0.31–0.45.

[40] The time variations of areas of cirrus clouds at the decaying stage of deep convection are studied by comparing the cloud size change in time in both the simulation and the split window analysis. We show that the areas of ice clouds in NICAM decay almost the same as satellite observations. This suggests that the fall speed of snow in this NICAM experiment is appropriate to depict the decay of anvil clouds by compensating for the excess of snow in NICAM simulations, when we assume that the decay of anvil clouds is largely controlled by the evaporation of ice and snow. This implication comes only from the results of a small number of case studies using the limited data of the simulation, and is far from conclusive. However, the significance of this study is that the combination of the comparisons of CFAD and of the time evolutions of cloud areas will lead to improvements in cloud microphysics schemes. Therefore, we will further

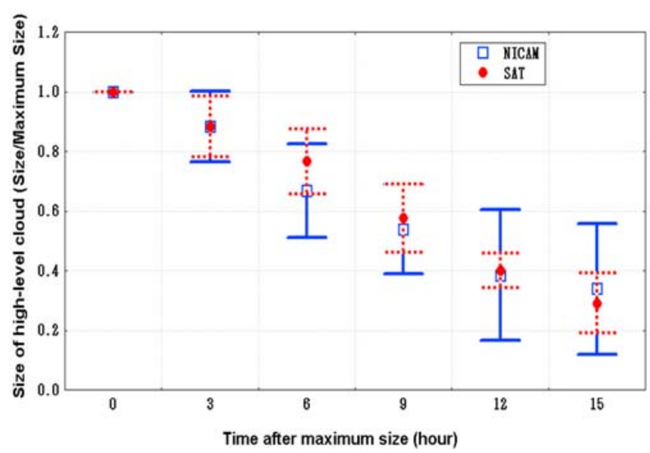

Figure 15. Temporal variation of high-level cloud area after the maximum size appeared during the life cycle of deep convection. The cloud area is represented as the ratio of area size to the maximum area size. Blue squares and bars indicate mean and standard deviations computed from 17 cases from NICAM, while red dots and bars indicate the same as blue for 11 cases from satellite observations.

explore systematic analysis using future GCRM experimental data.

[41] **Acknowledgments.** CALIPSO data were obtained from the NASA Langley Research Center Atmospheric Science Data Center. CloudSat data were provided by Colorado State University. We thank Mark Webb at the UK Met Office for the use of COSP. This research is supported by the program Core Research for Evolutional Science and Technology (CREST) under the Japan Science and Technology Agency (JST). The NICAM simulation was carried out using the Earth Simulator. This research is also supported by projects of JAXA/EarthCARE, MEXT/VL for Climate System Diagnostics, MOE/Global Environment Research Fund B-083, and NIES/GOSAT.

References

Ackerman, S. A., R. E. Holz, R. Frey, E. W. Eloranta, B. C. Maddux, and M. McGill (2008), Cloud detection with MODIS Part II: Validation, *J. Atmos. Oceanic Technol.*, *25*, 1073–1086, doi:10.1175/2007JTECHA1053.1.

Arakawa, A. (1975), Modeling clouds and cloud processes for use in climate models, in *The Physical Basis of Climate and Climate Modeling*, *GARP Pub. Ser.*, vol. 16, pp. 183–197, World Meteorol. Org., Geneva.

Bodas-Salcedo, A., M. J. Webb, M. E. Brooks, M. A. Ringer, K. D. Williams, S. F. Milton, and D. R. Wilson (2008), Evaluating cloud systems in the Met Office global forecast model using simulated CloudSat radar reflectivities, *J. Geophys. Res.*, *113*, D00A13, doi:10.1029/2007JD009620 [printed *114*(D8), 2009].

Chepfer, H., S. Bony, D. Winker, M. Chiriaco, J. L. Dufresne, and G. Seze (2008), Use of CALIPSO lidar observations to evaluate the cloudiness simulated by a climate model, *Geophys. Res. Lett.*, *35*, L15704, doi:10.1029/2008GL034207.

Davies, T., M. J. P. Cullen, A. J. Malcolm, M. H. Mawson, A. Staniforth, A. A. White, and N. Wood (2005), A new dynamical core for the Met Office's global and regional modeling of the atmosphere, *Q. J. R. Meteorol. Soc.*, *131*, 1759–1782, doi:10.1256/qj.04.101.

Grabowski, W. W. (1998), Toward cloud resolving modeling of large-scale tropical circulation: A simple cloud microphysics parameterization, *J. Atmos. Sci.*, *55*, 3283–3298, doi:10.1175/1520-0469(1998)055<3283:TCRMOL>2.0.CO;2.

Hamada, A., N. Nishi, S. Iwasaki, Y. Ohno, H. Kumagai, and H. Okamoto (2008), Cloud type and top height estimation for tropical upper-tropospheric clouds using GMS-5 split-window measurements combined with cloud radar measurements, *SOLA*, *4*, 57–60 doi:10.2151/sola.2008-015.

Haynes, J. M., R. T. Marchand, Z. Luo, A. Bodas-Salcedo, and G. L. Stephens (2007), A multi-purpose radar simulation package: QuickBeam, *Bull. Am. Meteorol. Soc.*, *88*, 1723–1727, doi:10.1175/BAMS-88-11-1723.

Heidinger, A. K., and M. J. Pavolonis (2009), Gazing at cirrus clouds for 25 years through a split window. Part 1: Methodology, *J. Appl. Meteorol. Clim.*, *48*, 1100–1116.

Horvath, A., and B. J. Soden (2008), Lagrangian diagnostics of tropical deep convection and its effect upon upper-tropospheric humidity, *J. Clim.*, *21*, 1013–1028, doi:10.1175/2007JCLI1786.1.

Illingworth, A. J., et al. (2007), CLOUDNET Continuous evaluation of cloud profiles in seven operational models using ground-based observations, *Bull. Am. Meteorol. Soc.*, *88*, 883–898, doi:10.1175/BAMS-88-6-883.

Inoue, T. (1985), On the temperature and effective emissivity determination of semi-transparent cirrus clouds by bi-spectral measurements in the 10 μm window region, *J. Meteorol. Soc. Jpn.*, *63*, 88–99.

Inoue, T. (1987), A cloud type classification with NOAA-7 split window measurements, *J. Geophys. Res.*, *92*, 3991–4000, doi:10.1029/JD092iD04p03991.

Inoue, T. (1989), Features of clouds over the tropical Pacific during northern hemisphere winter derived from split window measurements, *J. Meteorol. Soc. Jpn.*, *67*, 621–637.

Inoue, T. (1997), Day-to-night cloudiness change of cloud types inferred from split window aboard NOAA polar-orbiting satellite, *J. Meteorol. Soc. Jpn.*, *75*, 59–66.

Inoue, T., and S. Ackerman (2002), Radiative effect of various cloud types as classified by the split window technique over the eastern sub-tropical Pacific derived from collocated ERBE and AVHRR data, *J. Meteorol. Soc. Jpn.*, *80*, 1383–1394, doi:10.2151/jmsj.80.1383.

Inoue, T., M. Satoh, H. Miura, and B. Mapes (2008), Characteristics of cloud size of deep convection simulated by a global cloud resolving model, *J. Meteorol. Soc. Jpn.*, *86A*, 1–12. (Available at http://www.ccsr.u-tokyo.ac.jp/~satoh/paper/2008.Inoue/index.html)

Inoue, T., D. Vila, K. Rajendran, A. Hamada, X. Wu, and L. Machado (2009), Life cycle of deep convective systems over the eastern tropical Pacific observed by TRMM and GOES-W. J, *Meteorol. Soc. Jpn.*, *87A*, 381–391, doi:10.2151/jmsj.87A.381.

Kondo, Y. A. H., and K. Nakamura (2006), Small-scale cloud activity over the maritime continent and the western Pacific as revealed by satellite data, *Mon. Weather Rev.*, *134*, 1581–1599, doi:10.1175/MWR3132.1.

Liou, K.-N. (1986), Influence of cirrus clouds on weather and climate processes: A global perspective, *Mon. Weather Rev.*, *114*, 1167–1199, doi:10.1175/1520-0493(1986)114<1167:IOCCOW>2.0.CO;2.

Liu, Z., M. A. Vaughan, D. M. Winker, C. A. Hostetler, L. R. Poole, D. Hlavka, W. Hart, and M. McGill (2004), Use of probability distribution functions for discriminating between cloud and aerosol in lidar backscatter data, *J. Geophys. Res.*, *109*, D15202, doi:10.1029/2004JD004732.

Luo, Z., and W. B. Rossow (2004), Characterizing tropical cirrus life cycle, evolution, and interaction with upper-tropospheric water vapor using Lagrangian trajectory analysis of satellite observations, *J. Clim.*, *17*, 4541–4563, doi:10.1175/3222.1.

Mace, G. G., T. P. Ackerman, P. Minnis, and D. F. Young (1998a), Cirrus layer microphysical properties derived from surface-based millimeter radar and infrared interferometer data, *J. Geophys. Res.*, *103*, 23,207–23,216, doi:10.1029/98JD02117.

Mace, G. G., C. Jacob, and K. P. Morgan (1998b), Validation of hydrometeer occurrence predicted by the ECMWF model using millimeter wave radar data, *Geophys. Res. Lett.*, *25*, 1645–1648, doi:10.1029/98GL00845.

Machado, L., W. Rossow, R. Guedes, and A. Walker (1998), Life cycle variations of mesoscale convective systems over the Americas, *Mon. Weather Rev.*, *126*, 1630–1654, doi:10.1175/1520-0493(1998)126<1630:LCVOMC>2.0.CO;2.

Masunaga, H., M. Satoh, and H. Miura (2008), A joint satellite and global CRM analysis of an MJO event: Model diagnosis, *J. Geophys. Res.*, *113*, D17210, doi:10.1029/2008JD009986.

Minnis, P., K. N. Liou, and Y. Takano (1998), Inference of cirrus cloud properties using satellite-observed visible and infrared radiances. Part I: Parameterization of radiance fields, *J. Atmos. Sci.*, *55*, 3313–3339, doi:10.1175/1520-0469(1998)055<3313:PORAEE>2.0.CO;2.

Miura, H., M. Satoh, T. Nasuno, A. T. Noda, and K. Oouchi (2007), A Madden-Julian Oscillation event simulated using a global cloud-resolving model, *Science*, *318*, 1763–1765, doi:10.1126/science.1148443.

Nasuno, T., H. Miura, M. Satoh, A. T. Noda, and K. Oouchi (2009), Multi-scale organization of convection in a global numerical simulation of the December 2006 MJO event using explicit moist processes, *J. Meteorol. Soc. Jpn.*, *87*, 335–345.

Okamoto, H., S. Iwasaki, M. Yasui, H. Horie, H. Kuroiwa, and H. Kumagai (2003), An algorithm for retrieval of cloud microphysics using 95-GHz cloud radar and lidar, *J. Geophys. Res.*, *108*(D7), 4226, doi:10.1029/2001JD001225.

Palmer, T. N., F. J. Doblas-Reyes, A. Weisheimer, and M. J. Rodwell (2008), Toward seamless prediction: Calibration of climate change projections using seasonal forecasts, *Bull. Am. Meteorol. Soc.*, *89*, 459–470, doi:10.1175/BAMS-89-4-459.

Platt, C. M. R. (1979), Remote sensing of high clouds. I: Visible and infrared optical properties from lidar and radiometer measurements, *J. Appl. Meteorol.*, *18*, 1130–1143, doi:10.1175/1520-0450(1979)018<1130:RSOHCI>2.0.CO;2.

Prabhakara, C. R., S. Fraser, G. Dalu, M. L. C. Wu, R. J. Curran, and T. Styles (1988), Thin cirrus clouds: Seasonal distribution over oceans deduced from Nimbus-4 IRIS, *J. Appl. Meteorol.*, *27*, 379–399, doi:10.1175/1520-0450(1988)027<0379:TCCSDO>2.0.CO;2.

Rossow, W. B., and R. A. Schiffer (1991), ISCCP cloud data products, *Bull. Am. Meteorol. Soc.*, *72*, 2–20, doi:10.1175/1520-0477(1991)072<0002:ICDP>2.0.CO;2.

Sassen, K., C. D. Grund, J. D. Spinhirne, J. M. Alvarez, and M. J. Hardesty (1990), The 27–28 October 1986 FIRE IFO cirrus case study: A five lidar overview of cloud structure and evolution, *Mon. Weather Rev.*, *118*, 2288–2312, doi:10.1175/1520-0493(1990)118<2288:TOFICC>2.0.CO;2.

Satoh, M., T. Matsuno, H. Tomita, H. Miura, T. Nasuno, and S. Iga (2008), Nonhydrostatic Icosahedral Atmospheric Model (NICAM) for global cloud resolving simulations, *J. Comput. Phys.*, *227*, 3486–3514, doi:10.1016/j.jcp.2007.02.006.

Stephens, G. (2005), Cloud feedbacks in the climate system: A critical review, *J. Clim.*, *18*, 237–273, doi:10.1175/JCLI-3243.1.

Stephens, G. L., et al. (2002), The CLOUDSAT mission and the A-TRAIN, *Bull. Am. Meteorol. Soc.*, *83*, 1771–1790, doi:10.1175/BAMS-83-12-1771.

Stephens, G. L., et al. (2008), CloudSat mission: Performance and early science after the first year of operation, *J. Geophys. Res.*, *113*, D00A18, doi:10.1029/2008JD009982.

Tomita, H., and M. Satoh (2004), A new dynamical framework of nonhydrostatic global model using the icosahedral grid, *Fluid Dyn. Res.*, *34*, 357–400, doi:10.1016/j.fluiddyn.2004.03.003.

Winker, D. M., W. H. Hunt, and M. J. McGill (2007), Initial performance assessment of CALIOP, *Geophys. Res. Lett.*, *34*, L19803, doi:10.1029/2007GL030135.

World Meteorological Organization (2006), Implementation plan for a global Space-based inter-calibration system (GSICS), version 1, report, 22 pp., Geneva.

Wylie, D., P. Piironen, W. Wolf, and E. Eloranta (1995), Understanding satellite cirrus cloud climatologies with calibrated lidar optical depth, *J. Atmos. Sci.*, *52*, 4327–4343, doi:10.1175/1520-0469(1995)052<4327:USCCCW>2.0.CO;2.

Yuter, S. E., and R. A. Houze Jr. (2003), Microphysical modes of precipitation growth determined by S-band vertically pointing radar in orographic precipitation during MAP, *Q. J. R. Meteorol. Soc.*, *129*, 455–476, doi:10.1256/qj.01.216.

Y. Hagihara, Center for Atmospheric and Oceanic Studies, Tohoku University, Sendai 980-8578, Japan.

T. Inoue, H. Miura, and M. Satoh, Center for Climate System Research, University of Tokyo, 5-1-5 Kashiwanoha, Kashiwa-shi, Chiba 277-8568, Japan. (toshiro@ccsr.u-tokyo.ac.jp)

J. Schmetz, EUMETSAT, D-64295 Darmstadt, Germany.